ACS APPLIED NANO MATERIALS

www.acsanm.org Article

Visualizing Electric and Magnetic Field Coupling in Au-Nanorod Trimer Structures via Stimulated Electron Energy Gain and Cathodoluminescence Spectroscopy: Implications for Meta-Atom Imaging

David A. Garfinkel, Vasudevan Iyer, Robyn Seils, Grace Pakeltis, Marc R. Bourgeois, Andrew W. Rossi, Clay Klein, Benjamin J. Lawrie, David J. Masiello, and Philip D. Rack*

Cite This: *ACS Appl. Nano Mater.* 2022, 5, 1798–1807 Read Online

ACCESS | Metrics & More | Article Recommendations | Supporting Information

ABSTRACT: Trimer meta-atoms composed of three gold rods in an equilateral triangular geometry were fabricated, and their near-field plasmonic responses were characterized via electron energy loss (EEL), cathodoluminescence (CL), and stimulated electron energy loss/gain (sEEL/sEEG) spectroscopy. The trimer structure hybridizes into a low-energy mode with all three rods coupling in-phase, which produces a circulating current and thus a magnetic field. The next highest-energy mode consists of two rods coupling out-of-phase and produces a net electric dipole. We investigate the near fields of hybridized magnetic and electric modes via EEL and CL and correlate their spectral characteristics and intensity maps. Then, by changing the length of the trimer rods, we tune the magnetic and electric modes to our laser energy and characterize the excited state via sEEL/sEEG spectroscopy. Exploration of the tilt dependence, relative to the optical source, of the two modes reveals that the electric mode sEEG intensity increases more than the expected $\sin^2(\theta)$ dependence of the optical electric field coupling (see the Supporting Information for a detailed description). After correcting for the tail of the close-proximity electric mode, we demonstrate sEEG via coupling of the magnetic component of the optical field to the magnetic meta-atoms, which has the expected $\cos^2(\theta)$ tilt dependence. This realization opens the possibility to explore the nanoscale excited-state near-field imaging of other magnetic meta-atom structures.

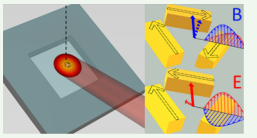

KEYWORDS: *plasmonic, magnetic dipole, trimer, meta-atom, electron energy spectroscopy*

INTRODUCTION

The quest for high-frequency magnetic materials has led to miniaturization of plasmonic meta-atom architectures. While standard split-ring resonator (SRR) geometries are useful meta-atoms for extension to infrared frequencies,[1,2] lithographic constraints make optical frequencies challenging.[3−5] Thus, coupled ring-like arrangements of nanospheres,[6−8] nanodisks,[9,10] and nanorods,[11−13] referred to as oligomers, have made it possible to extend magnetic modes to higher frequencies. Oligomers with an n number of nanoparticles or nanorods hybridize into localized surface plasmon (LSP) normal modes. For a system of nanorods arranged in a ring, the configuration with all individual longitudinal electric dipole LSPs orientated in-phase is the lowest energy mode, and the resultant circulating displacement current constitutes a magnetic dipole oriented normal to the closed loop. At higher energies, the individual electric dipoles arrange into different configurations, including those with a net electric dipole. The energy splitting between these modes is dependent on the individual oligomer length, spacing, and n.[14]

Several groups have studied the optical and magnetic resonances of nanoparticle ring structures [see ref 8 for review]. Alù et al.[15] showed theoretically that rings of silver nanoparticles can exhibit negative permeability and permittivity at optical frequencies where n, nanoparticle size and spacing, and the surrounding medium index of refraction all affect the resonance frequency. Experimentally, gold nanoshell particles were self-assembled, and the electric and magnetic dipole of an $n = 3$ nanoparticle cluster was revealed with p-polarization and s-polarization scattering measurements, respectively.[16] An atomic force microscope manipulation method was also used to direct the assembly of an $n = 4$ ring of gold nanoparticles, and oblique-angle scattering measurements with mixed s- and p-polarization induced both an electric and magnetic dipole.[17] Furthermore, slight geometric asymmetries were shown to enhance the magnetic dipole and lead to a Fano dip in the scattering spectra.[18] More recently, Morits and Simovski[19] showed that nanoparticle "dimers" that effectively prolate the sphere geometry enhanced the negative permittivity and permeability of $n = 4$ oligomers. Finally, the electric and magnetic dipoles of equilateral trimers of gold nanorods were also studied, and s-polarized excitation

Received: September 29, 2021
Accepted: January 20, 2022
Published: February 1, 2022

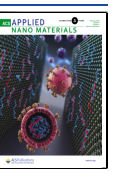

https://doi.org/10.1021/acsanm.1c03171
ACS Appl. Nano Mater. 2022, 5, 1798–1807

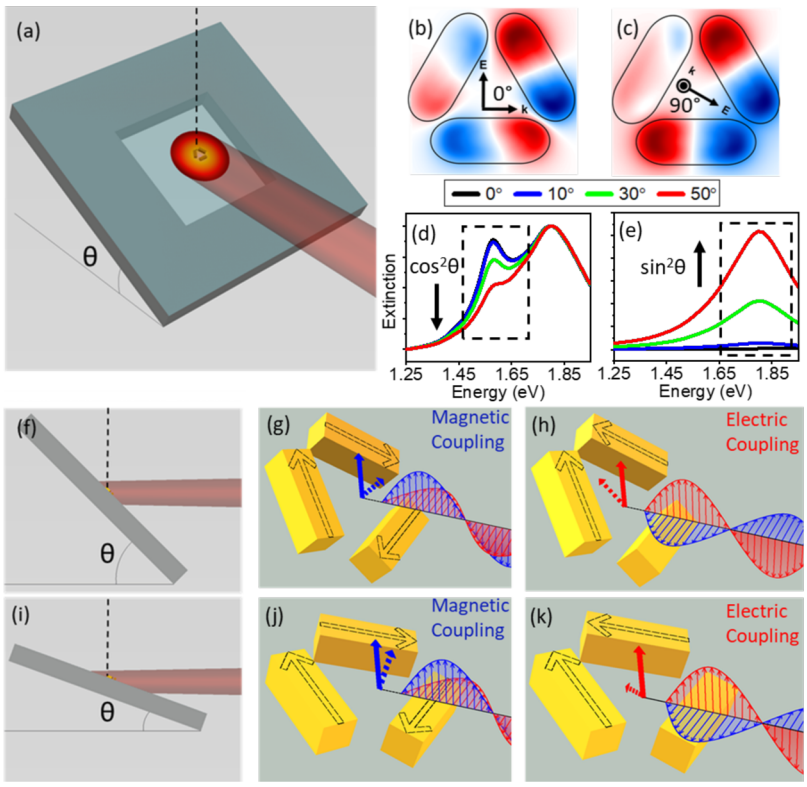

Figure 1. (a) Schematic of the sEEGS experimental setup, where θ indicates the sample tilt from the normal to the electron beam (shown as a dotted line in (a), (f), and (i)), and (b,c) calculated induced electric field maps of the magnetic and electric trimer modes with optical field orientations included as well as the laser-substrate angles relating the orientations to the plots directly below (d,e). In both cases, the normal component of the field at any integer multiple of the period is displayed; (f–k) influence of sample tilt on the optical coupling of the magnetic (g,j) and electric (h,k) modes. Black arrows indicate the direction of the individual nanorod dipole oscillation relative to the other nanorods. Red arrows are used to show the electric field, while blue is used for the magnetic field of the photon. Dotted red and blue arrows indicate that the projection of the electric and magnetic components onto the trimer substrate plane is operative.

clearly revealed both the electric and magnetic modes.[12] Again, slight geometric asymmetries in the structures enhance the magnetic dipole and can induce a Fano interference between the bright electric mode and the dark magnetic mode.

Electron energy loss spectroscopy (EELS) and cathodoluminescence spectroscopy (CL), leveraging high-spatial resolution near-field probes, have been used extensively to investigate various plasmonic phenomena [see refs 20 and 21 for recent reviews]. The hybridized in-phase and out-of-phase normal modes of a dimer have different spatial signatures that can be resolved with EELS spectrum imaging. Specifically, the in-phase vertices are more localized to the rod ends, whereas the out-of-phase modes exhibit a bright gap. Relevant to nanomagnetic plasmonic meta-atoms, von Cube et al. have studied individual[1,22] and coupled[23,24] SRRs. They realized infrared (1.25 eV) electric/magnetic dipole modes in gold SRRs with edge lengths down to 120 nm. The dispersion of gold surface plasmons and nanoscale synthesis limitations make it challenging to extend gold SRRs to optical frequencies. Barrow et al. assembled various trimer and tetramer symmetries of gold nanoparticles and characterized via EELS the various modes and confirmed the mode assignments via MNPBEM simulations.[25] EELS of silver nanorod equilateral triangles was recently studied, and the electric and magnetic dipole modes demonstrated an energy splitting of ∼0.25 eV.[11]

While CL of magnetic metamaterials has been more limited, chiral plasmonic nanostructures have been investigated.[26,27] Fang et al.[28] demonstrated contrast in the hot electron injection from 3d chiral SRRs for left- versus right-handed circular polarization. The dichroism was attributed to a hot spot in the thinnest region of the chiral SRR, which emerges when the handedness of the chiral SRR matches the handedness of circular polarized light. More recently, they also showed that the chirality of the CL from a heptamer structure was extremely sensitive to the electron beam position.[29] Correlative EELS and CL spectroscopy of three-dimensional SRRs was also performed to reveal various bright and dark modes, and complementary MNPBEM simulations were used to verify the mode assignments.[30]

To extend the capability of EELS, we have recently integrated an optical delivery system to a scanning transmission electron microscope (STEM) equipped with a monochromated electron source and an EELS detector. The laser delivery system is capable of photothermally heating the sample for in situ and so-called rapid ex situ imaging.[31] It can also be used to photoexcite the sample and thus enables photoinduced near-field imaging/spectroscopy of materials in a conventional microscope. For instance, we have demonstrated continuous wave (cw) stimulated EEL (sEEL) and stimulated EE gain (sEEG) signatures in silver nanostructures[32] and have characterized the longitudinal localized surface plasmon resonance (LSPR) modes (m = 1, 2, and 3) of gold nanorods[33] as well as coupled dimers.[34] While ultrafast time-resolved photoinduced near-field electron microscopy has been developed[35−38] and has elucidated interesting plasmonic[39,40] and biological processes,[41] the cw excitation of materials in a

https://doi.org/10.1021/acsanm.1c03171
ACS Appl. Nano Mater. 2022, 5, 1798−1807

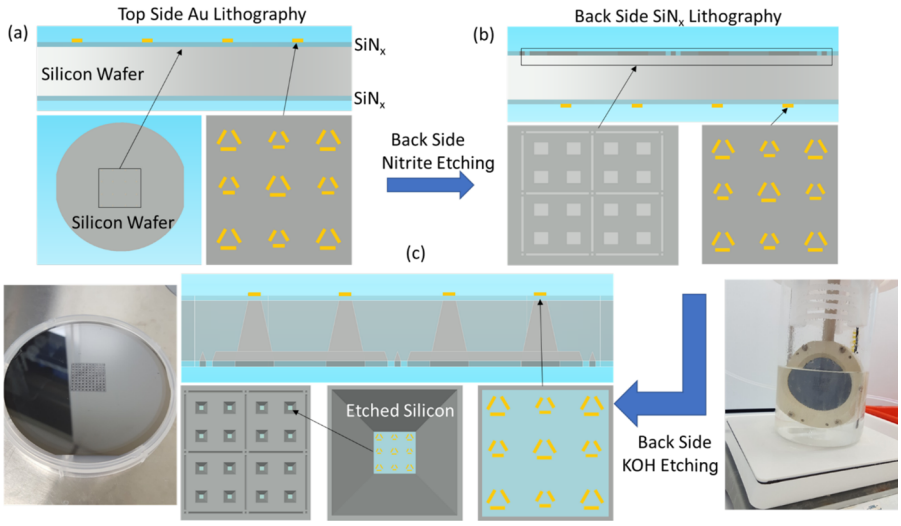

Figure 2. Sample fabrication process flow demonstrating the front side electron beam lithography and lift-off on the Si/SiN_x 300 μm-thick wafer (a), back side etching of the SiN_x mask layer (b), and finally removal of Si (c) to create an electron transparent membrane.

conventional microscope is useful for revealing many excited-state phenomena. In traditional EELS, all excitations of plasmonic modes are via spontaneous near-field interactions with the electron beam. Each individual event results in a loss of energy from the electron, and thus, the characteristic peaks occur on the loss side of the zero-loss peak. With simultaneous photoexcitation, plasmonic modes can be driven via photo-excitation, and thus, incident electrons can either gain or lose energy during near-field interactions, which leads to both sEEG and sEEL peaks with equal probability at the energy of the optical source and a full width at half-maximum (FWHM) equivalent to the electron source.

Here, we use EELS, CL, and sEEGS to map the near-field response of the two nondegenerate hybridized dipole modes in a simple plasmonic trimer structure. We use the conceptual framework of quasistatic mode solutions as the basis of interpreting our experiments and fully retarded numerical simulations. The magnetic dipole and doubly degenerate electric dipole modes[6] are clearly evident in the optical extinction spectra calculated using the discrete dipole approximation (Figure 1b,c). The lower-energy in-phase mode (Figure 1b) consists of the three longitudinal electric dipoles arranged in an in-phase configuration, leading to a circulating displacement current. In the remainder of the text, we will refer to this lowest energy mode as the magnetic mode (MD) due to the induced magnetic field. The doubly degenerate mode (Figure 1c), which will be referred to as the electric mode (ED) due to its net electric dipole, is composed of two rods coupled out-of-phase at a vertex and a near-zero longitudinal dipole moment for the remaining rod oriented perpendicular to the electric field polarization of the incident plane wave. To directly image the electric and magnetic modes of the trimer meta-atom in sEEGS, we vary the rod length to tune the magnetic and electric modes to the stimulating laser energy (1.58 eV). The trimer structure designed to align the magnetic mode with the laser energy will be referred to as the magnetic structure, while the trimer tuned to the electric mode will be referred to as the electric structure. Through the measurements of these two structures and variation of the tilt angle between the trimers and the laser, we visualize both electrically and magnetically driven optical coupling to plasmonic meta-atoms.

RESULTS AND DISCUSSION

Figure 1a schematically illustrates our experimental setup for sEEGS. Note that the electron beam (dashed line in Figure 1a) and the laser are fixed at a 90° angle relative to one another, so the sample must be tilted (θ) to focus both beams on the same field of view. Figure 1b,c shows calculated electric field maps of the magnetic and electric modes, respectively. Figure 1b demonstrates the reduced intensity of the electric field in the gap position associated with the circulating in-phase configuration (magnetic mode), while Figure 1c shows the high intensity in the gap from an out-of-phase vertex (bottom right vertex) in the electric mode. Figure 1d (s-polarization) and Figure 1e (p-polarization) show the simulated behaviors of two different optical orientations demonstrating the tilt dependence of magnetically and electrically driven optical coupling. Both the lower-energy magnetic peak (1.58 eV) and the higher-energy electric peak (1.80 eV) can be excited with s-polarization, whereas only the electric mode is observed with p-polarization. As is shown in Figure 1d, the magnetic mode under s-polarization decreases with $\cos^2(\theta)$, and in Figure 1e under p-polarization, the electric mode increases with $\sin^2(\theta)$. Figure 1f,i shows two tilt angles (θ) to illustrate the influence that tilt has on coupling between the trimers and the laser. This is shown as both s- (Figure 1g,j) and p- (Figure 1h,k) polarizations to indicate magnetic (s-polarization) and electric (p-polarization) field stimulation of the trimer meta-atom. Our laser source is unpolarized, so a combination of electric and magnetic optical coupling is observed in an integrated sEEG experiment. With this experimental setup, θ is typically constrained to a range of about ~20−35° due to interference from the silicon membrane frame at large angles and the difficulty in aligning the laser at lower angles. Figure 1h,k illustrates that coupling between the electric component of the optical field and the electric mode is increased (the magnitude of the projected component, illustrated as a red dotted arrow) as θ increases (i.e., where the electric field is $\propto \sin(\theta)$ and the intensity is $\propto \sin^2(\theta)$). For the magnetic mode (Figure 1g,j), where there is no net electric dipole for electric field coupling, the magnetic dipole is oriented normal to the structure, and thus, increasing the tilt angle reduces the coupling strength of the magnetic component of the optical field (shown by the

https://doi.org/10.1021/acsanm.1c03171
ACS Appl. Nano Mater. 2022, 5, 1798−1807

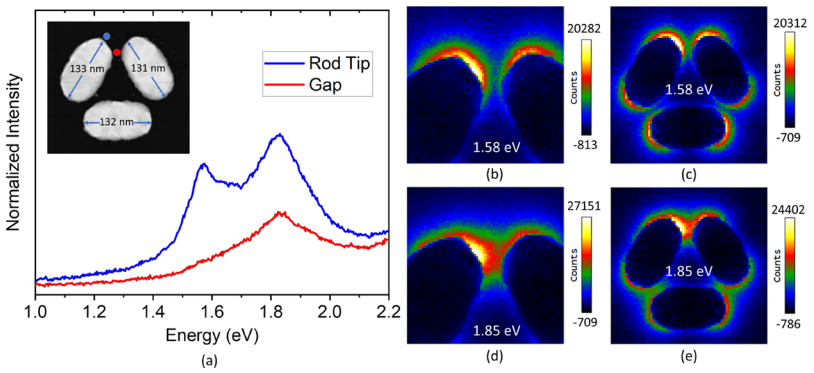

Figure 3. (a) High-resolution point spectra at a tip and gap aloof position. (b,c) Intensity maps of the magnetic mode at 1.58 eV for the top vertex (b) and the whole trimer (c) and the electric mode at 1.85 eV for the top vertex (d) and the whole trimer (e).

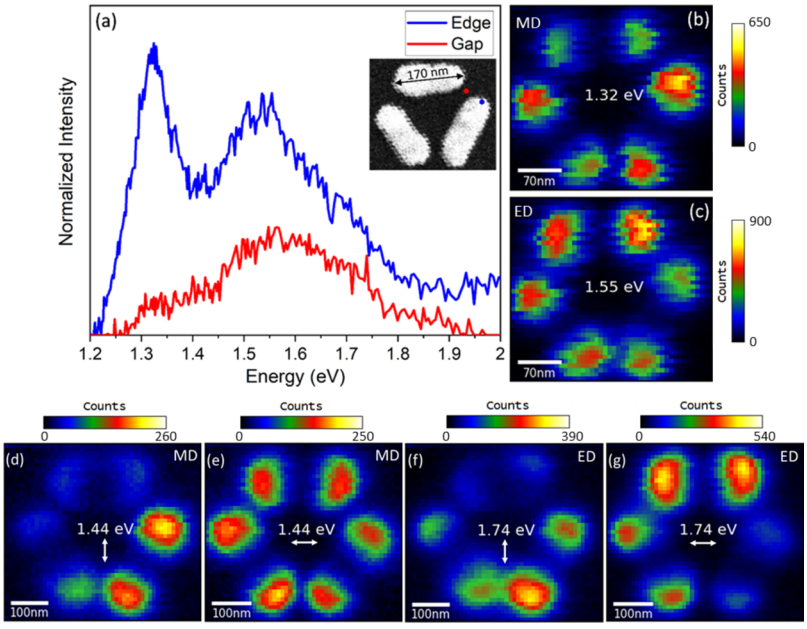

Figure 4. (a) CL spectra showing a gap position (red) and an edge position (blue) (SEM image inset), (b,c) intensity maps at energies corresponding to the magnetic (b) and electric modes (c), and (d−g) intensity maps of the magnetic (MD) and electric (ED) modes with vertical (d,f) and horizontal (e,g) polarization filtering on a different trimer structure with a similar orientation to the inset SEM image in (a).

dotted blue arrow, where the magnetic field is $\propto \cos(\theta)$ and the intensity is $\propto \cos^2(\theta)$). Thus, by modifying the tilt angle, the relative optical coupling strength of each mode varies inversely.

The small spatial dimensions required to tune the magnetic and electric modes of gold trimer structures to our 1.58 eV laser necessitated high-resolution electron beam lithography. The complexity of the sample preparation was enhanced by the need of an electron transparent substrate for EELS. The process used to fabricate these gold meta-atoms is illustrated in Figure 2. Figure 2a demonstrates the first step, which is traditional electron beam lithography and lift-off on a 300 μm-thick silicon wafer coated with 30 nm of SiN_x to create the trimer structures on one side of the wafer (the front side). The electron transparent substrate was then achieved via multistep lithography and etching, shown in Figure 2b,c. Additional details on the sample fabrication are included in the Methods section.

Prior to performing excited-state spectroscopy on the trimers, a separate instrument was used to obtain high-energy resolution (20 meV FWHM) EELS data on a sample trimer structure with rod lengths of 131, 132, and 133 nm. The high-energy resolution measurements are conducted to clearly demonstrate the energy splitting of the two spontaneous EELS peaks, as the inferior energy resolution associated with the sEEGS experiments obscures this distinction. Figure 3 demonstrates the hybridization of the three longitudinal electric dipole rod LSPs into the electric and magnetic normal modes through point spectra (a) and intensity maps (b−e). As illustrated by the high-angle annular dark-field (HAADF) inset, the point spectra were taken at two positions, in between the two rods at the vertex (gap) and at the end of one of the rods (tip). At the tip position, both the magnetic (1.58 eV) and the electric (1.85 eV) modes are excited; conversely, in the gap, the magnetic mode is greatly reduced due to symmetry selection rules. The intensity maps of the full structure (c and e), as well as the magnified top vertex (b and d), clearly reinforce the observations from the point spectra. Whereas the electric mode has a high intensity at the gap, the magnetic mode has a characteristic nodal line in the gap center where decay in the intensity is much sharper for the magnetic mode than the electric mode.

https://doi.org/10.1021/acsanm.1c03171
ACS Appl. Nano Mater. 2022, 5, 1798−1807

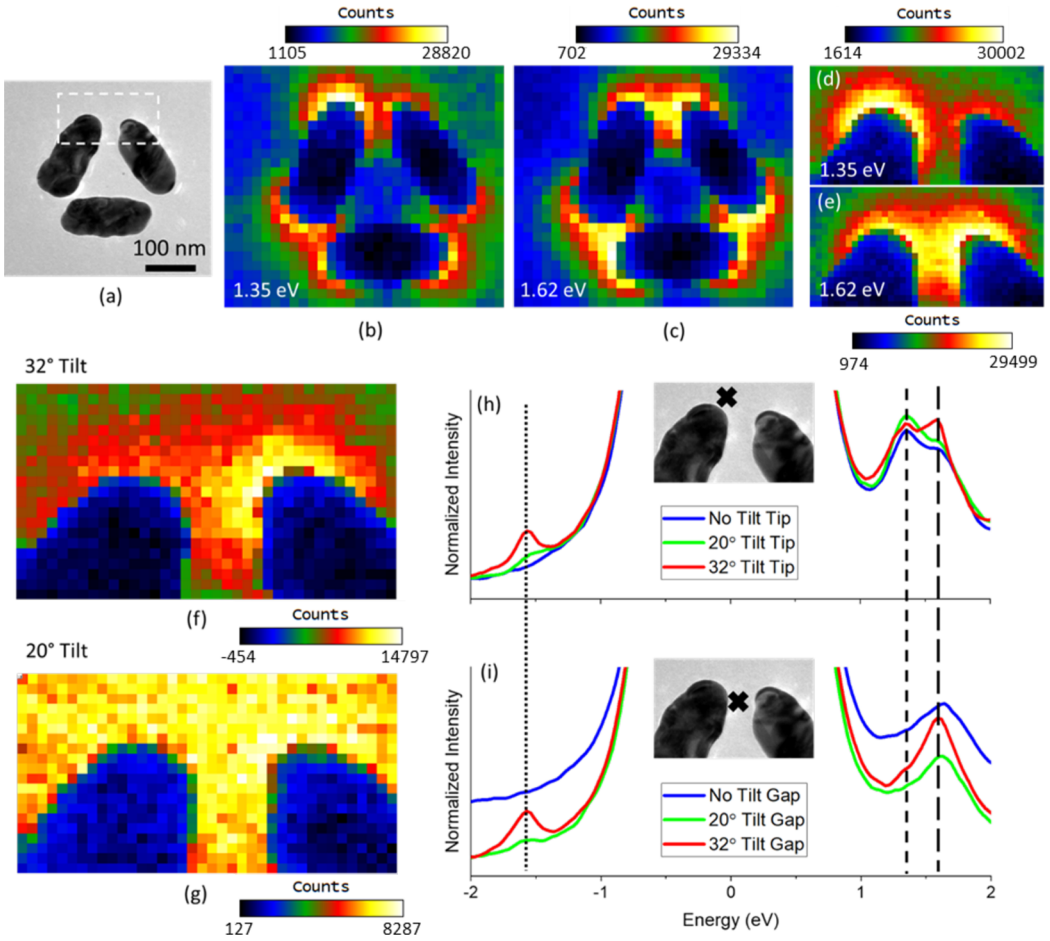

Figure 5. (a) TEM bright-field image of a trimer that hybridizes with the electric dipole resonant near the stimulating laser energy. The measured rod lengths are ∼175 nm. (b,c) Intensity maps of the magnetic (1.35 eV) and electric (1.62) dipole modes. (d,e) High-spatial resolution intensity map of the top vertex from (b) and (c). (f,g) sEEGS intensity maps of the vertex in (d) and (e) at −1.58 eV with the laser on at 20 and 32° tilts. (h,i) Point spectra of the trimer at no tilt with no laser irradiance and with the laser on with 20 and 32° tilts taken at the rod tip (h) and the gap (i).

While EELS is the electron beam analog to optical extinction, CL is the electron beam analog to optical scattering. Thus, to complement high-energy resolution EELS, we performed CL as it also enables a high-energy resolution measurement of the electric and magnetic modes. A separate trimer structure with rod lengths of 170, 168, and 176 nm was characterized using CL as shown in Figure 4a−c. Note that the CL intensity is much lower than the EELS intensity and results in a lower signal-to-noise ratio. Here, there is an expected red-shift associated with an increase in the rod length compared to Figure 3, leading to a resonant energy of 1.32 eV for the magnetic mode and 1.55 eV for the electric mode. As was observed in Figure 3, the excitation of both modes is observed at the rod tip, whereas only the electric mode is observed in the gap position. The intensity maps in Figure 4b,c exhibit a slightly more localized high intensity area at the rod tips in the magnetic mode compared to a higher intensity in the gap position in the electric mode. Note that the jagged edges in the intensity maps in Figure 4b,c are scan artifacts associated with the necessarily long pixel dwell times. A polarization study on a different, but similarly oriented, trimer is included in Figure 4d−g. In this polarization-filtered setup, the electron beam excites all modes as the impact parameter is raster scanned over the sample; however, only photons, which fulfill the polarization requirements, are collected. When only vertically polarized light is collected, the top rod is almost entirely dark for both modes as the dipole associated with this rod has a negligible vertical component. Horizontal polarization collection exhibits a uniform excitation in all individual rods for the magnetic mode, as all rods have a horizontal dipole component. In the electric mode, the horizontal rod demonstrates the greatest intensity as it is well-aligned with the horizontal polarization. As can be seen in Figure 4f, the right rod has a higher intensity with vertical polarization, so in turn, the left rod has a higher intensity in horizontal polarization. This is likely the result of a slight clockwise rotation of the polarizers relative to vertical and horizontal orientations illustrated.

Trimers with rod lengths of ∼175 nm were fabricated to efficiently tune the electric dipole mode to our 1.58 eV stimulating laser source. Figure 5a shows a bright-field TEM image of the electric structure. The associated EELS intensity maps without laser irradiance at the magnetic mode (1.35 eV) and the electric mode (1.62 eV) are shown in Figure 5b,c, respectively. Figure 5d,e shows higher-spatial resolution intensity maps of the top vertex as illustrated by the white dashed box in Figure 5a. The overall trends observed in Figure 3, namely, the variation in the signatures between the two modes, are consistent with what is observed in Figure 5a−e. The primary deviation is the greater asymmetry in the magnetic mode of the trimer characterized in Figure 5. Here, the left rod in the top vertex (seen in both (b) and (d)) has a

https://doi.org/10.1021/acsanm.1c03171
ACS Appl. Nano Mater. 2022, 5, 1798−1807

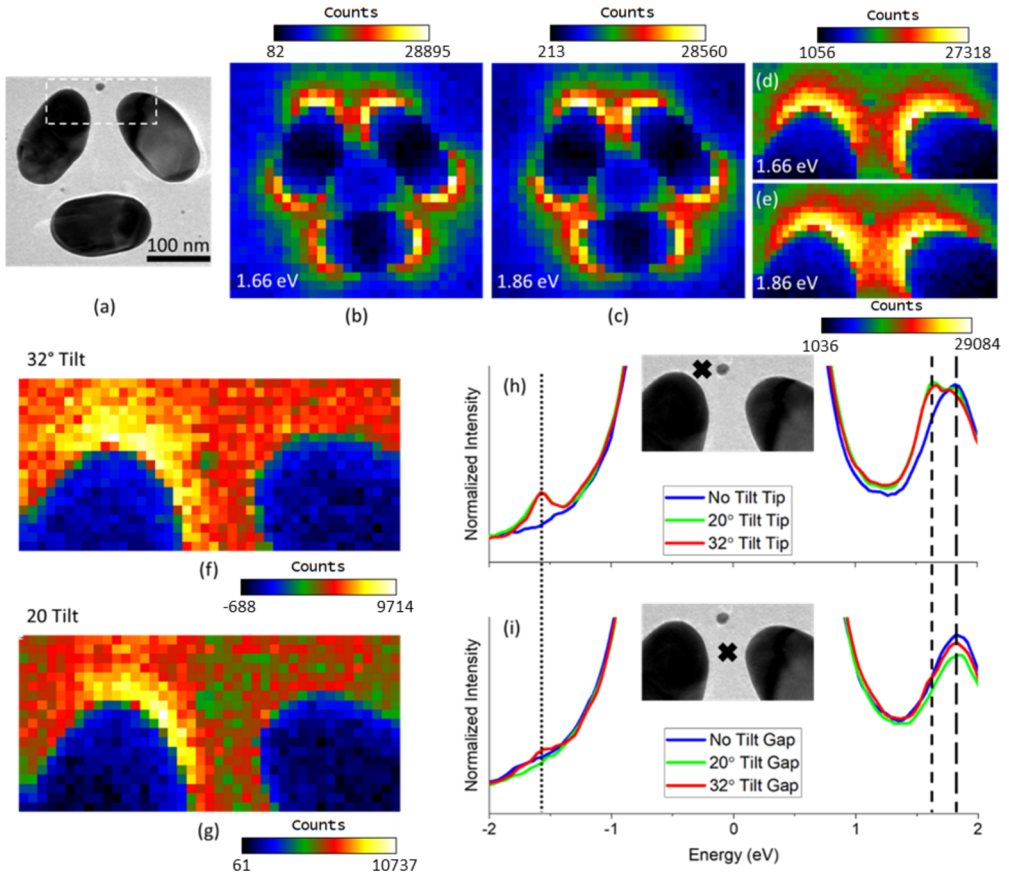

Figure 6. (a) TEM bright-field image of a trimer that hybridizes with the magnetic dipole resonant near the laser energy. The measured rod lengths are ∼140 nm. (b,c) Intensity maps of the magnetic (1.66 eV) and electric (1.86) dipole modes. (d,e) High-spatial resolution intensity maps of the top vertex from (b) and (c). (f,g) sEEGS intensity maps of the vertex in (d) and (e) at −1.58 eV with the laser on at 20 and 32° tilts. (h,i) Point spectra of the trimer at no tilt with no laser irradiance and with the laser on with 20 and 32° tilts taken at the rod tip (h) and the gap (i).

greater intensity in the magnetic mode than the remainder of the structure. Conversely, the excitation of the electric mode appears to be slightly higher near the right rod, though this result is subtle. Both of these features can be attributed to slight asymmetries in the trimer structures.

As our excitation irradiance is in a regime in which the plasmon occupation number is less than one, the gain/loss spectrum consists of a convolution of the ground-state spontaneous EEL peaks and the sEEL and sEEG peaks. In the sEEGS experimental setup, the top vertex is the farthest point from the laser, which empirically leads to the largest sEEG signal. While the nonuniformities are not fully understood, similar effects have been observed in photoemission electron microscopy and have been correlated to retardation effects as well as asymmetries in the electric field induced at the vacuum and substrate interface due to oblique angle excitation.[42,43] Because of the enhanced emission, higher-spatial resolution sEEGS experiments were measured at the top vertex of the trimers. Specifically, intensity maps of the vertex (Figure 5f,g) and point spectra at a tip and gap aloof position (Figure 5h,i) were collected at tilt angles of 20 and 32° and a laser irradiance of 1.3×10^5 W/cm^2. Intensity maps filtered at −1.58 eV with the structure tilted at 20 (Figure 5g) and 32° (Figure 5f) demonstrate the tilt sensitivity of sEEGS. At 20°, the intensity from the sEEG peak is low and not discernible above the noise level. When the sample tilt is increased to 32°, the electric component of the optical field increases and the sEEGS signature increases. Peak intensities are observed near the rod tips, with a maximum near the right rod, which is consistent with the elevated EELS intensity at the same rod tip without laser irradiance (Figure 5e). Figure 5h,i shows EELS point spectra taken at zero tilt (no laser), as well as at 20 and 32° tilts with the laser on. An aloof position in the gap is shown in Figure 5i, while an aloof position at the rod tip is shown in Figure 5h. The sEEG (dotted line), magnetic (short dashed line), and electric (long dashed line) peak positions are indicated. The increased collection time associated with point spectra compared to intensity maps results in a peak at −1.58 eV for both tilt conditions and both aloof positions, indicating coupling to the stimulating optical field. The gain behavior is strikingly similar in the two aloof positions: there is a clear increase, of similar magnitude to the sEEG intensity with an increasing tilt angle. The loss behavior, however, is quite different and consistent with what is observed in Figure 3a: the ratio of the electric mode to the magnetic mode is much greater in the gap than at the tip. The lack of sensitivity in the sEEGS peak to the magnetic mode suggests that there is a minimal contribution from the detuned magnetic mode (ΔE = 0.23 eV from laser energy) in the electric structure.

The magnetic mode was tuned to the laser energy via patterning trimers with slightly reduced rod lengths of ∼140 nm. Similar to Figure 5, Figure 6 shows a bright-field TEM image (a) and associated intensity maps of the complete trimer ((b) and (c)) and the top vertex ((d) and (e)) at the magnetic mode (1.66 eV) and electric mode (1.86 eV) energies with no laser irradiance. The behavior of this trimer is very similar to

https://doi.org/10.1021/acsanm.1c03171
ACS Appl. Nano Mater. 2022, 5, 1798−1807

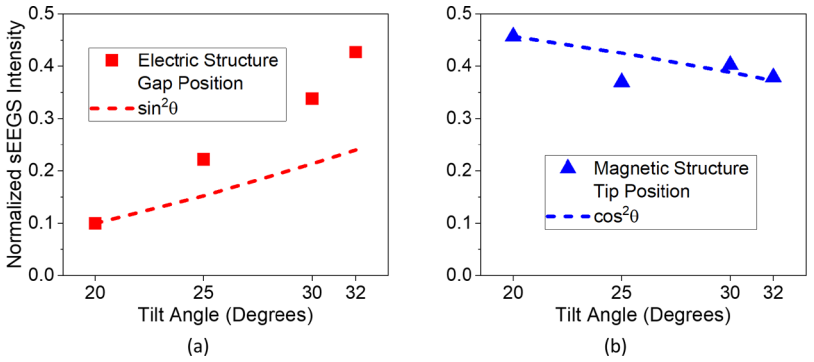

Figure 7. (a) sEEGS intensity at −1.58 eV in the gap position of the electric structure normalized by the intensity of the spontaneous electric dipole mode at 1.58 eV demonstrating electrically stimulated optical coupling. The red dashed line indicates the expected increasing $\sin^2(\theta)$ behavior. (b) sEEGS intensity at −1.58 eV for the tip position of the magnetic structure normalized by the intensity of the spontaneous magnetic mode with the electric coupling contributions removed to demonstrate optical coupling stimulated by the magnetic component of the optical field. The blue dashed line indicates the expected decreasing $\cos^2(\theta)$ behavior.

that of the electric structure; however, the energy splitting between the two modes is reduced (0.2 eV compared to 0.27 eV), and the magnetic structure exhibits a more symmetric intensity map at the top vertex.

sEEGS measurements are presented in Figure 6 for the magnetic structure where the sample was tilted again to 20 and 32° with a laser irradiance of 1.3×10^5 W/cm^2. At both tilt conditions, the sEEGS intensity maps (Figure 6f,g) show obvious indications of optical coupling to the magnetic structure. The peak intensity is more localized to the left rod. Because the laser is tuned to the magnetic dipole, the tip position has a larger sEEG peak (Figure 6h) compared to the gap position (Figure 6i). As will be explained below, the tip position sEEG intensities at the two angles have similar intensities.

To better elucidate the electric and magnetic optical field coupling stimulating the electric and magnetic dipole modes, we further explore the sEEGS tilt dependence of the two modes. As previously discussed,[32−34] the sEEG intensity is proportional to the product of the spontaneous EELS intensity, the laser irradiance, and the extinction cross section of the LSPR mode at the laser energy. As shown in ref 33, the spontaneous EELS intensity for rods aligned parallel to the tilt axis slightly decreases with increasing θ and remains constant for rods aligned perpendicular to the tilt axis. The spontaneous EELS intensity is also sensitive to the aloof position, which can vary slightly during experimentation. Thus, to understand the optical coupling to the trimer meta-atom, it is convenient to normalize the sEEGS intensity by the magnitude of the spontaneous EELS intensity at the laser energy [see the Supporting Information for peak fitting and normalization of each mode at all tilt angles, including intermediate tilt angles of 25 and 30°]. This in principle corrects for the angular dependence of the spontaneous EELS as well as any differences in the aloof position, which typically varies exponentially with the distance from the rod end. Figure 7a shows a plot of the normalized sEEG intensity of the electric structure measured at the gap position where any contribution from the magnetic mode is negligible. The normalized sEEG intensity increases with increasing θ as expected for the coupling of the electric component of the optical field to the electric dipole LSPR. Interestingly, the increase in intensity supersedes the predicted $\sin^2(\theta)$ tilt behavior, which is shown as a red dashed line in the figure.

To investigate the tilt angle dependence of the magnetic mode, the sEEGS intensity is again normalized by the spontaneous EELS peak at the laser energy for the tip aloof position on the magnetic structure. As illustrated in the SI, the intensity of the spontaneous electric dipole mode is nonzero at the laser energy, so we subtract this contribution to reveal the pure magnetic mode coupling. Figure 7b shows a plot of the resultant normalized sEEGS intensity versus θ, which has the expected decreasing $\cos^2(\theta)$ dependence (blue dashed line) and thus confirms the magnetic component coupling of the optical field to the meta-atom.

It is peculiar that the normalized electric mode sEEG intensity tilt dependence exceeds the expected $\sin^2(\theta)$ dependence. While the exact cause is not understood at this time, we speculate that two effects could be playing a role. First of all, asymmetries in plasmon oligomers[12,17,18] are known to modify the near-field optical properties, where both spectral and scattering efficiencies are affected. Clearly, the lithographically patterned structures have slight differences in the rod lengths, widths, heights, and gaps, which could result in complicated in-plane and out-of-plane near-field distributions. Second, our previous model[33] ignores substrate effects, which also perturb the optically induced and electron-induced LSP near-field distribution.[44,45] Thus, the observed behavior of the normalized electric mode could be due to either, or a combination, of these effects. To elucidate these contributions, various future studies are proposed: (1) comparing oligomers on substrates with different indices of refraction, (2) intentionally patterning various oligomer asymmetries, and (3) exploring different laser energies to probe different spectral regions.

CONCLUSIONS

Gold nanorods were patterned in a trimer configuration with sufficiently small gaps to induce the hybridization of the individual rods into a collective lower-energy in-phase magnetic dipole mode and an out-of-phase electric dipole mode. The nanoscale characteristic EEL and CL spectra and intensity maps were correlated to the expected near-field distributions of the meta-atom hybridized modes. Two trimer structures were fabricated to tune the electric mode and the magnetic mode to our stimulating laser energy, and the sEEG spectra and intensity maps were characterized as a function of the tilt angle. By tilting the trimers, we can probe whether the

https://doi.org/10.1021/acsanm.1c03171
ACS Appl. Nano Mater. 2022, 5, 1798−1807

electric or magnetic component of the optical field is stimulating the LSPR mode tuned to the laser energy. The normalized sEEGS peak increases more than the expected $\sin^2(\theta)$ dependence when coupled to the electric dipole mode of the trimer meta-atom. The normalized sEEGS intensity tuned to the magnetic mode of the trimer meta-atom had the expected $\cos^2(\theta)$ dependence. Thus, we have shown that sEEGS is capable of probing and visualizing the near field of electrically and magnetically driven plasmonic meta-atoms.

METHODS

Fabrication. The gold trimer structures were fabricated through a multistep lithography process. Using electron beam lithography, arrays of trimers with different rod lengths and gap sizes were patterned on a 300 μm silicon wafer with 30 nm low-stress SiN_x coating on both sides. Metal deposition of approximately 40 nm-thick gold was done via direct current sputtering; lift-off was completed through sonicated baths of alternating acetone and microdeposit remover 1165. To obtain electron transparent membranes beneath these metalized areas, silicon was removed with wet etching in a KOH bath. An S1818 photoresist was used to create a mask in which the desired membrane areas on the back side of the wafer could be etched using a SiN_x dry etching process. The wafer was then placed in a fixture that protects the metalized side via an air cavity, while the back side with areas of exposed silicon was left open to the environment. This fixture was submerged in a KOH bath at 85 °C until the silicon was completely removed from unmasked areas (~5 h). Finally, individual TEM samples each with four ~100 × 100 μm 30 nm SiN_x membranes supporting the gold trimer structures were cleaved. This process is illustrated in Figure 2.

High-Energy Resolution EELS. A Nion aberration-corrected high-energy resolution monochromated EELS-STEM (HERMES) operated at an accelerating voltage of 60 kV with a Nion Iris spectrometer was used to obtain individual point spectra and intensity maps. The convergence and collection semiangles used for the spectrum acquisition were 30 and 15 mrad, respectively, and the beam current was 20 pA. The energy resolution (full width at half-maximum of the zero-loss peak) was approximately 20 meV with an energy dispersion of 3 meV. A zero-loss peak normalization was used on the EEL spectra shown in Figure 3. Intensity maps were generated with an energy window of ±51 meV. The large overview maps have a pixel size of 3.6 nm, while the vertex maps have a pixel size of 2 nm. An acquisition time of 0.1 s was used, and for point spectra, a total of 50 frames were summed.

Cathodoluminescence Microscopy. Cathodoluminescence microscopy was performed with a Delmic Sparc cathodoluminescence module installed on a FEI Quattro environmental scanning electron microscope. All reported CL data utilized a beam energy of 30 kV, beam currents of 0.5−2 nA, and integration times of 1 s for spectrum images and 25 s for point spectra. Intensity maps utilized an energy window of ±15 meV. The Sparc module comprises a 0.9 numerical aperture parabolic mirror that directs collected cathodoluminescence to an Andor Kymera 193i spectrometer with a 150 lines/mm grating and a Newton CCD camera. Achromatic waveplates and polarizers were used to enable arbitrary control over the measured polarization state.

Stimulated Electron Energy Loss and Gain Spectroscopy. A Zeiss Libra with a 785 nm solid-state laser oriented normal to the electron beam was used for EELS and sEELS/sEEGS measurements. An acceleration voltage of 200 kV, a spot size of 200 pm, a collection semiangle of 30 mrad, and a convergence semiangle of 10 mrad were used. A dispersion of 30 meV per channel was obtained via a 0.5 μm monochromator slit. An exposure time of 0.07 s was used for both point spectra and intensity maps. A total of 10 frames were summed for the point spectra resulting in a total of 0.7 s. The pixel size in the intensity maps varied slightly for each measurement due to minor changes in the selected area; however, the pixel size for all vertex intensity maps was 2.5 ±0.2 nm. The zero-tilt no-laser intensity maps of the complete magnetic and electric structures were 5.9 and 6.1 nm, respectively. An energy range of ±61 meV was used for all intensity maps. During measurements, a spatial drift compensation after each completed row was used for all intensity maps, though thermal drift was minimal during measurements due to providing ample time for the sample to reach equilibrium following changes to the tilt. Excited-state imaging was conducted with an irradiance of 1.3×10^5 W/cm^2 in the 5 μm Gaussian laser spot.

Peak Fitting. Fitting of the spontaneous and stimulated EE peak raw data was completed in a method similar to previous sEEGS experiments.[31,32] First, the raw data was normalized to the zero-loss peak, then a Gaussian function was fitted to the zero-loss peak, and this peak was subtracted. Next, the SiN_x background was removed by a combination of four Lorentzian peaks. The sEEGS peak was fitted by removing the tail left by the zero-loss peak with the tail of a Lorentzian function and then via a single Lorentzian function with an inputted position of −1.58 eV (the laser energy) and the previously determined full width at half-maximum from the zero-loss peak. For the loss peaks, the tail from the zero-loss peak was removed using an exponential decay fit. The peak positions for the electric and magnetic modes were then determined by fitting the flat no-laser EELS spectra, where no sEELS peak was present to obscure the data in any way, at both the tip and gap positions. For excited-state spectra, after removing the zero-loss peak tail, the sEELS peak was removed by subtracting the sEEGS peak mirrored to 1.58 eV. Finally, using the peak positions obtained from the flat, no-laser irradiance spectra, the two modes were fitted to two Lorentzian functions, with two additional Lorentzian peaks fitting the gold quasiplanar peak at ~2.4 eV and any remnants from the SiN_x background removal. Additional information on peak fitting can be found in the Supporting Information.

Discrete Dipole Approximation Simulations. All simulations were performed using version 7.1 of the discrete dipole approximation (DDA) code[46] with a background refractive index of unity (ignoring the bottom SiN_x substrate) and a dipole spacing of 2 nm. The gold trimer structures were composed of rods 165 nm in length, 60 nm in width, and 30 nm in thickness. The dielectric data was taken from Johnson and Christy.[47] In panels (b) and (c) of Figure 1, the component of the electric field normal to the plane of the trimer is plotted at a fixed distance of 12 nm above the top surface of the rods. The color bar represents E_z/max(E_z) in the 2D evaluation plane, where z is the direction normal to the trimer plane. The field maps in panels (b) and (c) of Figure 1 were plotted at an energy corresponding to the maxima of the MD and ED modes observed in panels (d) and (e), respectively.

ASSOCIATED CONTENT

Supporting Information

The Supporting Information is available free of charge at https://pubs.acs.org/doi/10.1021/acsanm.1c03171.

Additional information on the peak fitting process, resultant fits from each measurement, STEM images showing the top vertex of the trimers at three tilt conditions, and additional information on the tilt dependence of the trimers (PDF)

AUTHOR INFORMATION

Corresponding Author

Philip D. Rack − *Department of Materials Science and Engineering, University of Tennessee, Knoxville, Tennessee 37996, United States; Center for Nanophase Materials Sciences, Oak Ridge National Laboratory, Oak Ridge, Tennessee 37831, United States;* orcid.org/0000-0002-9964-3254; Email: prack@utk.edu

https://doi.org/10.1021/acsanm.1c03171
ACS Appl. Nano Mater. 2022, 5, 1798−1807

Authors

David A. Garfinkel − *Department of Materials Science and Engineering, University of Tennessee, Knoxville, Tennessee 37996, United States;* orcid.org/0000-0002-7593-1868

Vasudevan Iyer − *Center for Nanophase Materials Sciences, Oak Ridge National Laboratory, Oak Ridge, Tennessee 37831, United States;* orcid.org/0000-0002-2722-7630

Robyn Seils − *Department of Materials Science and Engineering, University of Tennessee, Knoxville, Tennessee 37996, United States*

Grace Pakeltis − *Department of Materials Science and Engineering, University of Tennessee, Knoxville, Tennessee 37996, United States;* orcid.org/0000-0003-1478-4654

Marc R. Bourgeois − *Department of Chemistry, University of Washington, Seattle, Washington 98195, United States;* orcid.org/0000-0002-9435-9051

Andrew W. Rossi − *Department of Chemistry, University of Washington, Seattle, Washington 98195, United States;* orcid.org/0000-0001-7588-534X

Clay Klein − *Department of Physics, Clarion University of Pennsylvania, Clarion, Pennsylvania 16214, United States*

Benjamin J. Lawrie − *Center for Nanophase Materials Sciences, Oak Ridge National Laboratory, Oak Ridge, Tennessee 37831, United States;* orcid.org/0000-0003-1431-066X

David J. Masiello − *Department of Chemistry, University of Washington, Seattle, Washington 98195, United States;* orcid.org/0000-0002-1187-0920

Complete contact information is available at: https://pubs.acs.org/10.1021/acsanm.1c03171

Notes

The authors declare no competing financial interest.

■ ACKNOWLEDGMENTS

D.A.G., R.S., G.P., and P.D.R. acknowledge support from the National Science Foundation under grant NSF DMR 1709275. P.D.R. acknowledges that the laser delivery system was built by Tom Moore and Greg Magel at Waviks, Inc. and the system development is supported by NSF SBIR-1721719 and 1853201. Work at the University of Washington was supported by the U.S. National Science Foundation under Award CHE-1954393 (M.R.B., A.W.R., and D.J.M.). All the authors acknowledge that the nanofabrication, high-energy resolution EELS measurements, and CL were conducted at the Center for Nanophase Materials Sciences, which is a DOE Office of Science User Facility.

■ REFERENCES

(1) von Cube, F.; Irsen, S.; Niegemann, J.; Matyssek, C.; Hergert, W.; Busch, K.; Linden, S. Spatio-Spectral Characterization of Photonic Meta-Atoms with Electron Energy-Loss Spectroscopy [Invited]. *Opt. Mater. Express* **2011**, *1*, 1009−1018.

(2) Zhou, J.; Koschny, T.; Kafesaki, M.; Economou, E. N.; Pendry, J. B.; Soukoulis, C. M. Saturation of the Magnetic Response of Split-Ring Resonators at Optical Frequencies. *Phys. Rev. Lett.* **2005**, *95*, 223902.

(3) Tobing, L. Y. M.; Tjahjana, L.; Zhang, D. H.; Zhang, Q.; Xiong, Q. Sub-100-Nm Sized Silver Split Ring Resonator Metamaterials with Fundamental Magnetic Resonance in the Middle Visible Spectrum. *Adv. Opt. Mater.* **2014**, *2*, 280−285.

(4) Enkrich, C.; Wegener, M.; Linden, S.; Burger, S.; Zschiedrich, L.; Schmidt, F.; Zhou, J. F.; Koschny, T.; Soukoulis, C. M. Magnetic Metamaterials at Telecommunication and Visible Frequencies. *Phys. Rev. Lett.* **2005**, *95*, 203901.

(5) Tomioka, T.; Kubo, S.; Nakagawa, M.; Hoga, M.; Tanaka, T. Split-Ring Resonators Interacting with a Magnetic Field at Visible Frequencies. *Appl. Phys. Lett.* **2013**, *103*, No. 071104.

(6) Brandl, D. W.; Mirin, N. A.; Nordlander, P. Plasmon Modes of Nanosphere Trimers and Quadrumers. *J. Phys. Chem. B* **2006**, *110*, 12302−12310.

(7) Zohar, N.; Chuntonov, L.; Haran, G. The Simplest Plasmonic Molecules: Metal Nanoparticle Dimers and Trimers. *J. Photochem. Photobiol., C* **2014**, *21*, 26−39.

(8) Monticone, F.; Alù, A. The Quest for Optical Magnetism: From Split-Ring Resonators to Plasmonic Nanoparticles and Nanoclusters. *J. Mater. Chem. C* **2014**, *2*, 9059−9072.

(9) Hentschel, M.; Dorfmüller, J.; Giessen, H.; Jäger, S.; Kern, A. M.; Braun, K.; Zhang, D.; Meixner, A. J. Plasmonic Oligomers in Cylindrical Vector Light Beams. *Beilstein J. Nanotechnol.* **2013**, *4*, 57−65.

(10) Reich, S.; Mueller, N. S.; Bubula, M. Selection Rules for Structured Light in Nanooligomers and Other Nanosystems. *ACS Photonics* **2020**, *7*, 1537−1550.

(11) Cherqui, C.; Wu, Y.; Li, G.; Quillin, S. C.; Busche, J. A.; Thakkar, N.; West, C. A.; Montoni, N. P.; Rack, P. D.; Camden, J. P.; Masiello, D. J. STEM/EELS Imaging of Magnetic Hybridization in Symmetric and Symmetry-Broken Plasmon Oligomer Dimers and All-Magnetic Fano Interference. *Nano Lett.* **2016**, *16*, 6668−6676.

(12) Greybush, N. J.; Pacheco-Peña, V.; Engheta, N.; Murray, C. B.; Kagan, C. R. Plasmonic Optical and Chiroptical Response of Self-Assembled Au Nanorod Equilateral Trimers. *ACS Nano* **2019**, *13*, 1617−1624.

(13) Li, Z.-J.; Wu, Z.-S.; Li, H.-Y. Analysis of Electromagnetic Scattering by Uniaxial Anisotropic Bispheres. *J. Opt. Soc. Am. A* **2011**, *28*, 118−125.

(14) Pakeltis, G.; Rotunno, E.; Khorassani, S.; Garfinkel, D. A.; Collette, R.; West, C. A.; Retterer, S. T.; Idrobo, J. C.; Masiello, D. J.; Rack, P. D. High Spatial and Energy Resolution Electron Energy Loss Spectroscopy of the Magnetic and Electric Excitations in Plasmonic Nanorod Oligomers. *Opt. Express* **2021**, *29*, 4661−4671.

(15) Alù, A.; Salandrino, A.; Engheta, N. Negative Effective Permeability and Left-Handed Materials at Optical Frequencies. *Opt. Express* **2006**, *14*, 1557−1567.

(16) Fan, J. A.; Wu, C.; Bao, K.; Bao, J.; Bardhan, R.; Halas, N. J.; Manoharan, V. N.; Nordlander, P.; Shvets, G.; Capasso, F. Self-Assembled Plasmonic Nanoparticle Clusters. *Science* **2010**, *328*, 1135−1138.

(17) Shafiei, F.; Monticone, F.; Le, K. Q.; Liu, X.-X.; Hartsfield, T.; Alù, A.; Li, X. A Subwavelength Plasmonic Metamolecule Exhibiting Magnetic-Based Optical Fano Resonance. *Nat. Nanotechnol.* **2013**, *8*, 95−99.

(18) Sheikholeslami, S. N.; García-Etxarri, A.; Dionne, J. A. Controlling the Interplay of Electric and Magnetic Modes via Fano-like Plasmon Resonances. *Nano Lett.* **2011**, *11*, 3927−3934.

(19) Morits, D. K.; Simovski, C. R. Negative Effective Permeability at Optical Frequencies Produced by Rings of Plasmonic Dimers. *Phys. Rev. B* **2010**, *81*, 205112.

(20) Wu, Y.; Li, G.; Camden, J. P. Probing Nanoparticle Plasmons with Electron Energy Loss Spectroscopy. *Chem. Rev.* **2018**, *118*, 2994−3031.

(21) Coenen, T.; Haegel, N. M. Cathodoluminescence for the 21st Century: Learning More from Light. *Appl. Phys. Rev.* **2017**, *4*, No. 031103.

(22) Boudarham, G.; Feth, N.; Myroshnychenko, V.; Linden, S.; De Abajo, J. G.; Wegener, M.; Kociak, M. Spectral Imaging of Individual Split-Ring Resonators. *Phys. Rev. Lett.* **2010**, *105*, 255501.

(23) Von Cube, F.; Irsen, S.; Diehl, R.; Niegemann, J.; Busch, K.; Linden, S. From Isolated Metaatoms to Photonic Metamaterials: Evolution of the Plasmonic near-Field. *Nano Lett.* **2013**, *13*, 703−708.

(24) Liang, Q.; Wen, Y.; Mu, X.; Reindl, T.; Yu, W.; Talebi, N.; Van Aken, P. A. Investigating Hybridization Schemes of Coupled Split-

Ring Resonators by Electron Impacts. *Opt. Express* **2015**, *23*, 20721−20731.
(25) Barrow, S. J.; Collins, S. M.; Rossouw, D.; Funston, A. M.; Botton, G. A.; Midgley, P. A.; Mulvaney, P. Electron Energy Loss Spectroscopy Investigation into Symmetry in Gold Trimer and Tetramer Plasmonic Nanoparticle Structures. *ACS Nano* **2016**, *10*, 8552−8563.
(26) Hachtel, J. A.; Davidson, R. B.; Kovalik, E. R.; Retterer, S. T.; Lupini, A. R.; Haglund, R. F.; Lawrie, B. J.; Pantelides, S. T. Polarization- and Wavelength-Resolved near-Field Imaging of Complex Plasmonic Modes in Archimedean Nanospirals. *Opt. Lett.* **2018**, *43*, 927−930.
(27) Hachtel, J. A.; Cho, S.-Y.; Davidson, R. B., II; Feldman, M. A.; Chisholm, M. F.; Haglund, R. F.; Idrobo, J. C.; Pantelides, S. T.; Lawrie, B. J. Spatially and Spectrally Resolved Orbital Angular Momentum Interactions in Plasmonic Vortex Generators. *Light: Sci. Appl.* **2019**, *8*, 33.
(28) Fang, Y.; Verre, R.; Shao, L.; Nordlander, P.; Käll, M. Hot Electron Generation and Cathodoluminescence Nanoscopy of Chiral Split Ring Resonators. *Nano Lett.* **2016**, *16*, 5183−5190.
(29) Han, T.; Zu, S.; Li, Z.; Jiang, M.; Zhu, X.; Fang, Z. Reveal and Control of Chiral Cathodoluminescence at Subnanoscale. *Nano Lett.* **2018**, *18*, 567−572.
(30) Bicket, I. C.; Bellido, E. P.; Meuret, S.; Polman, A.; Botton, G. A. Correlative Electron Energy Loss Spectroscopy and Cathodoluminescence Spectroscopy on Three-Dimensional Plasmonic Split Ring Resonators. *Microsc.* **2018**, *67*, i40−i51.
(31) Wu, Y.; Liu, C.; Moore, T. M.; Magel, G. A.; Garfinkel, D. A.; Camden, J. P.; Stanford, M. G.; Duscher, G.; Rack, P. D. Exploring Photothermal Pathways via *in Situ* Laser Heating in the Transmission Electron Microscope: Recrystallization, Grain Growth, Phase Separation, and Dewetting in $Ag_{0.5}Ni_{0.5}$ Thin Films. *Microsc. Microanal.* **2018**, *24*, 647−656.
(32) Liu, C.; Wu, Y.; Hu, Z.; Busche, J. A.; Beutler, E. K.; Montoni, N. P.; Moore, T. M.; Magel, G. A.; Camden, J. P.; Masiello, D. J.; Duscher, G.; Rack, P. D. Continuous Wave Resonant Photon Stimulated Electron Energy-Gain and Electron Energy-Loss Spectroscopy of Individual Plasmonic Nanoparticles. *ACS Photonics* **2019**, *6*, 2499−2508.
(33) Collette, R.; Garfinkel, D. A.; Hu, Z.; Masiello, D. J.; Rack, P. D. Near Field Excited State Imaging via Stimulated Electron Energy Gain Spectroscopy of Localized Surface Plasmon Resonances in Plasmonic Nanorod Antennas. *Sci. Rep.* **2020**, *10*, 12537.
(34) Collette, R.; Garfinkel, D. A.; Rack, P. D. Nearfield Excited State Imaging of Bonding and Antibonding Plasmon Modes in Nanorod Dimers via Stimulated Electron Energy Gain Spectroscopy. *J. Chem. Phys.* **2020**, *153*, No. 044711.
(35) Zewail, A. H. Four-Dimensional Electron Microscopy. *Science* **2010**, *328*, 187−193.
(36) Howie, A. New Instrumentation and Cutting Edge Research. *Ultramicroscopy* **2017**, *180*, 52−58.
(37) Shorokhov, D.; Zewail, A. H. Perspective: 4D Ultrafast Electron Microscopy—Evolutions and Revolutions. *J. Chem. Phys.* **2016**, *144*, No. 080901.
(38) Barwick, B.; Zewail, A. H. Photonics and Plasmonics in 4D Ultrafast Electron Microscopy. *ACS Photonics* **2015**, *2*, 1391−1402.
(39) Yurtsever, A.; Baskin, J. S.; Zewail, A. H. Entangled Nanoparticles: Discovery by Visualization in 4D Electron Microscopy. *Nano Lett.* **2012**, *12*, 5027−5032.
(40) Barwick, B.; Flannigan, D. J.; Zewail, A. H. Photon-Induced near-Field Electron Microscopy. *Nat. Cell Biol.* **2009**, *462*, 902−906.
(41) Lu, Y.; Yoo, B.-K.; Ng, A. H. C.; Kim, J.; Yeom, S.; Tang, J.; Lin, M. M.; Zewail, A. H.; Heath, J. R. 4D Electron Microscopy of T Cell Activation. *Proc. Natl. Acad. Sci. U. S. A.* **2019**, *116*, 22014−22019.
(42) Ji, B.; Wang, Q.; Song, X.; Tao, H.; Dou, Y.; Gao, X.; Hao, Z.; Lin, J. Disclosing Dark Mode of Femtosecond Plasmon with Photoemission Electron Microscopy. *J. Phys. D: Appl. Phys.* **2017**, *50*, 415309.
(43) Yang, J.; Sun, Q.; Yu, H.; Ueno, K.; Misawa, H.; Gong, Q. Spatial Evolution of the Near-Field Distribution on Planar Gold Nanoparticles with the Excitation Wavelength across Dipole and Quadrupole Modes. *Photon. Res.* **2017**, *5*, 187−193.
(44) Mazzucco, S.; Stéphan, O.; Kociak, M.; Geuquet, N.; Henrard, L.; Ye, J.; Van Roy, W.; Van Dorpe, P. Ultralocal Modification of Surface Plasmons Properties in Silver Nanocubes. *Nano Lett.* **2012**, *12*, 1288−1294.
(45) Li, G.; Cherqui, C.; Wu, Y.; Bigelow, N. W.; Simmons, P. D.; Rack, P. D.; Masiello, D. J.; Camden, J. P. Examining Substrate-Induced Plasmon Mode Splitting and Localization in Truncated Silver Nanospheres with Electron Energy Loss Spectroscopy. *J. Phys. Chem. Lett.* **2015**, *6*, 2569−2576.
(46) Draine, B. T.; Flatau, P. J. Discrete-Dipole Approximation For Scattering Calculations. *J. Opt. Soc. Am. A* **1994**, *11*, 1491−1499.
(47) Johnson, P. B.; Christy, R. W. Optical Constants of the Noble Metals. *Phys. Rev. B* **1972**, *6*, 4370−4379.

https://doi.org/10.1021/acsanm.1c03171
ACS Appl. Nano Mater. 2022, 5, 1798−1807